

Deconvolution Techniques for Passive Radar Imaging

Aaron D. Lanterman^a and David C. Munson, Jr.^b

^aSchool of Electrical and Computer Engineering Georgia Institute of Technology,
Mail Code 0250, Atlanta, GA 30332

^bCoordinated Science Laboratory, Univ. of Illinois
1308 W. Main, Urbana, IL 61801

ABSTRACT

Forming images of aircraft using passive radar systems that exploit “illuminators of opportunity,” such as commercial television and FM radio systems, involves reconstructing an image from sparse samples of its Fourier transform. For a given flight path, a single receiver-transmitter pair produces one arc of data in Fourier space. Since the resulting Fourier sampling patterns bear a superficial resemblance to those found in radio astronomy, we consider using deconvolution techniques borrowed from radio astronomy, namely the CLEAN algorithm, to form images from passive radar data.

Some deconvolution techniques, such as the CLEAN algorithm, work best on images which are well-modeled as a set of distinct point scatterers. Hence, such algorithms are well-suited to high-frequency imaging of man-made targets, as the current on the scatterer surface tends to collect at particular points. When using low frequencies of interest in passive radar, the images are more distributed. In addition, the complex-valued nature of radar imaging presents a complication not present in radio astronomy, where the underlying images are real valued. These effects conspire to present a great challenge to the CLEAN algorithm, indicating the need to explore more sophisticated techniques.

Keywords: passive radar, radar imaging, CLEAN algorithm, missing data

1. INTRODUCTION

Traditional radar systems transmit waveforms and deduce information about targets by measuring and analyzing the reflected signals. The active nature of such radars can be problematic in military scenarios since the transmission reveals both the existence and location of the transmitter. An alternative approach is to exploit “illuminators of opportunity” such as commercial television and AM and FM radio broadcasts. Such passive approaches offer numerous advantages. The overall system cost may be cheaper, since a transmitter is no longer needed. Commercial transmitters are typically much higher in elevation than the prevailing terrain, yielding coverage of low altitude targets. Most importantly, such a system may remain covert, yielding increased survivability and robustness against deliberate directional interference.

Exploiting commercial broadcasts, however, has certain drawbacks. The reflected signal may be up to 130 dB lower than the direct-path signal, so receiver circuitry with high dynamic range and high-precision analog-to-digital converters are needed.

An NTSC television signal, for instance, places approximately 85 percent of its energy in the carrier. Unlike a conventional radar, the signal is not “pulsed”; essentially, the waveform consists mostly of a sinusoid which is on *all the time*. Thus, while trying to extract range information from television signals is a mostly hopeless task, a good deal of information about velocity is available via the resulting doppler shift of the carrier. FM radio signals can provide some range information, but still with far less resolution than can be obtained from a pulsed signal.

Television and FM radio broadcasts operate at wavelengths that are much larger than those typically employed in active radar systems. For instance, an X-band radar might operate at 10 GHz, whereas a passive radar system operates in the VHF and UHF bands (55-885 MHz). From an imaging viewpoint, lower frequencies result in

reduced cross-range resolution; hence, to achieve high-resolution images, the target needs to be tracked for some length of time to obtain data over a wide range of angles.

Some passive radar systems, such as Lockheed Martin’s Silent Sentry, have been created, which can detect and track targets. This paper focuses on issues involving formation of radar images from such passive radar data.

2. TOMOGRAPHIC FORMULATION OF MULTISTATIC RADAR

In many traditional active imaging systems, repetitions of a stepped or swept frequency waveform are transmitted, with each repetition viewing the target from a different angle. As analyzed in Ref. 1, the complex nature of reflectance (in particular, the lack of phase correlation from pixel-to-pixel) permits superb reflectance reconstructions even from a small range of angles. The driving force of the tomographic paradigm is the projection-slice theorem, which indicates that the data from different look angles yield different “slices” of the 2-D or 3-D Fourier transform at different angles through the origin, and the stepped-frequency waveform provides the samples of the Fourier transform along those slices.

In a bistatic scenario, the equivalent “look angle” is the bisector of the angle formed by the receiver-target-transmitter triangle.^{2,3} The part of this slice that is provided depends on the transmitted signal. Unfortunately, relatively low effective bandwidth signals available in passive scenarios will provide only a single point along the slice. In a monostatic case, the position of this point is determined solely by the frequency of the transmitted signal. In our bistatic case, the ellipses of constant path length become increasingly dense as the bistatic angle β increases. Essentially, as the bistatic angle increases, the Fourier sample slides towards the origin. If the target lies along the baseline ($\beta = \pi$), then only a DC component is provided.

Individual television and FM radio stations are relatively narrowband when compared to the bandwidths typically employed in imaging radar. At each instant, each transmitter-receiver pair provides one point in the 2-D frequency spectrum. Multiple television stations must be exploited to obtain the frequency diversity needed for reasonable-quality imaging. In addition, the aircraft must be tracked and data collected over time to obtain angular diversity, with each transmitter-receiver pair providing data on a circular arc in 2-D Fourier space.

2.1. Analogy with Radio Astronomy

There is a close relation between our passive radar imaging scenario and radio astronomy. Since the genesis of interferometric radio astronomy, researchers have exploited the connection between measurements of the signal correlation between receiver pairs and the Fourier transform of the scene being imaged. Basically, each correlation measurement gives an estimate of one point of that Fourier transform. The position of the point in Fourier space depends on the vector separation of the two antennas associated with that measurement. By changing the position of the array elements (either by physically moving the elements or by waiting for the Earth to rotate), additional points may be obtained, but it is almost impossible to obtain all the points needed to form a good image by direct Fourier inversion. Simply setting the missing points to zero and applying an inverse Fourier transform yields a blurry image with complicated sidelobe structures, often called the “dirty map.” In addition, negative pixel values are often obtained, even though the intensity being reconstructed should be nonnegative. Radio astronomers rely on two main tools, the CLEAN algorithm^{4,5} and maximum entropy,^{6,7} to produce useful “clean maps.” Although the underlying mapping between the correlation data and the intensity map is linear, CLEAN and maximum entropy algorithms are both nonlinear forms of processing.

Although the underlying physics that lead to a Fourier model in radar imaging is quite different from that leading to the Fourier model in radio astronomy, the Fourier sampling patterns in both problems bear a striking resemblance. This suggests that some of the methods used in radio astronomy might prove useful in the passive radar imaging scenario. There are, however, a few fundamental differences which should be kept in mind:

- Fourier sampling patterns in radio astronomy have a symmetry relationship $F(u, v) = F(-u, -v)$ which implies that the associated point-spread function (PSF) is real-valued. No such relationship in general holds in the radar scenario, and hence the PSF is complex-valued.

- Although radio astronomy measurements are based on coherent interferometry, the underlying astronomical sources radiate incoherently. Hence, the intensity being reconstructed is not only real, but nonnegative as well; this information can be exploited in the image reconstruction algorithm. Radar reflectances, on the other hand, are complex-valued. Although often only the magnitude is displayed to the human analyst (or fed to an automatic target recognition system), complicated phase relationships often have an underappreciated effect on the imaging process. In particular, complex scatterers, when blurred with a complex PSF, can interfere with each other in intricate constructive or destructive ways.

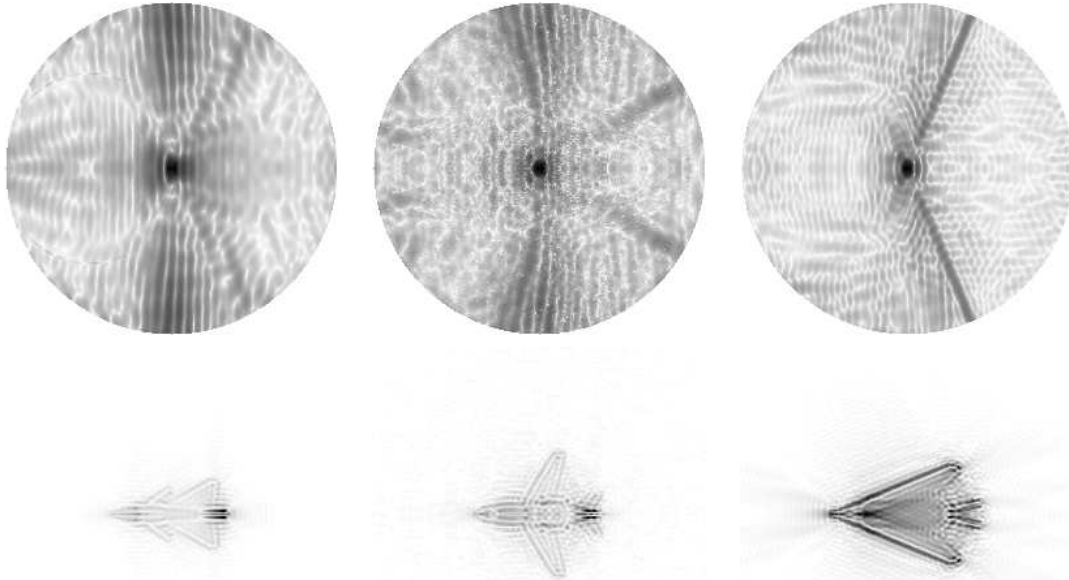


Figure 1. Fourier data (top row) from all incident and observed angles for a 211.25 MHz signal, along with corresponding radar images (bottom row) created using direct Fourier reconstruction. Left to right: VFY-218, Falcon 20, Flying Bat. The actual radar images are 512×512 ; here only the middle 256×256 pixels are shown.

2.2. Electromagnetic Simulation via FISC

Asymptotic codes such as XPATCH do not work well for aircraft-sized targets at the low frequencies of interest in passive radar systems. Hence, the simulations in the remaining sections invoke the Fast Illinois Solver Code (FISC), which solves Maxwell’s equations via the method of moments. FISC is extremely particular about the quality of CAD models it needs. In particular, FISC requires that each edge of each triangular facet exactly match the edge of some other triangular facet. The model must contain no internal or intersecting parts. Unfortunately, such models are rare; in particular, readily available models which are perfectly adequate for XPATCH are often not suitable for FISC.

Each experiment in this paper is conducted on three different targets: a VFY-218, a Dassault Falcon 20, and a Flying Bat. A FISC compatible model of the VFY-218 comes standard as part of the SAIC Champaign XPATCH/FISC distribution. In addition, a Falcon 100 model purchased from Viewpoint Digital happened to be FISC compatible. The Falcon 20 is essentially a larger version of the Falcon 100, so we created an approximate Falcon 20 model by scaling the Falcon 100 model. The Flying Bat was constructed by the first author from sources purchased at a hobby shop; for that model, coordinates were painstakingly read off of scans in Photoshop and typed into a text file by hand.

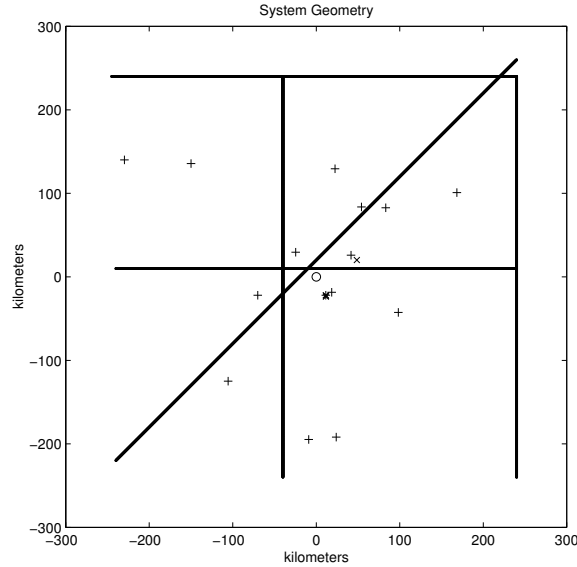


Figure 2. Data collection geometry. VHF TV stations are represented with a +; FM radio stations with a ×, and the receiver with a circle. The lines represent five hypothetical flight paths.

2.3. Direct Fourier Reconstruction from Full Datasets

The top row of Fig. 1 shows Fourier data corresponding to 211.25 MHz (NTSC television channel 13) and incident and observed angles over the full 360 degree viewing circle for three different targets: a VFY-218, a Dassault Falcon 20, and a Flying Bat model. Although such rich data sets would be entirely unavailable in practice, images reconstructed with such complete data sets give us a kind of “upper bound” on expected imaging performance. The magnitudes of radar images created by inverse Fourier transforming the data in the top row of Fig. 1 are shown in the second row of Fig. 1.

The tomographic radar model suggests that bistatic data at one frequency can be used to synthesize data at multiple lower frequencies. In the initial studies reported later in this paper, we will approximate passive radar data for a variety of transmitted frequencies using the Fourier datasets shown in shown in the top row of Fig. 1, constructed using FISC runs at the single frequency 211.15 MHz. Illuminators using a lower frequency effectively give points further towards the origin of the grid. (A similar approach was a taken in Ref. 8.) Although this is convenient because it allows us to isolate the sparse-sampling effect and tackle it in the absence of other complicating effects (such as frequency-dependent and angle-dependent scattering characteristics), it is important to check whether this bistatic frequency-equivalence trick is valid. Simply zeroing all Fourier data at radial frequencies over 100 MHz in the 211.25 MHz data sets in the top row of Fig. 1 might provide a reasonable estimate (shown in the first row of Fig. 3) of the data which might be collected if an actual frequency of 100 MHz was used (shown in the second row of Fig. 3). Some subtle differences can be seen between the two resulting Fourier datasets, suggesting that whereas there is a near equivalence, it would be wise not to push the tomographic model too far. Inverse Fourier transform reconstructions from the datasets in the first and second rows of Fig. 3 are shown in the third and fourth rows, respectively. While the resulting images are not the same, they are similar.

2.4. Direct Fourier Reconstruction from Sparse Datasets

Figure 2 shows the locations of 7 VHF television stations and 15 FM radio stations in the Washington DC area assumed in our simulations. The center of the coordinate system, where our hypothetical receiver is located, is the Lockheed Martin Mission Systems facility in Gaithersburg, MD. Five hypothetical flight paths are shown. The top row of Fig. 4 shows Fourier sampling patterns resulting from this particular transmitter/receiver geometry and for each of the five flight paths. The other two columns show the magnitude of the corresponding PSFs

given by the inverse Fourier transform of the sampling patterns. The middle column shows magnitude on a linear scale, while the right column shows magnitude on a logarithmic scale given by $\log(x + 10^{-3})$ to elucidate low-level detail in the sidelobes.

Direct Fourier inversion of the data from the top row of Fig. 1, multiplied by the mask of the left column of Fig. 4, results in the images displayed in Fig. 5. Fourier points where data is unavailable are set to zero. This is equivalent to convolving the images in the bottom row of Fig. 1 with the PSFs in the middle row of Fig. 4. There is a row-to-row correspondence between Figs. 4 and 5.

Observe that the images in the bottom three rows of Fig. 5, while blurry, are far clearer than the images in the top two rows. Looking at the corresponding sampling patterns, the primary difference seems to be that the paths corresponding to the top two rows keep the receiver and the transmitters on the same side of the target, yielding a quasi-monostatic (small bistatic angle) geometry, whereas in the bottom three rows, the target flies between the receiver and some of the transmitters, yielding large bistatic angles and wider effective coverage in frequency space.

At first glance, this would suggest that we should chose geometries that ensure large bistatic angles. In particular, this is easily achieved in geometries where targets fly between the transmitter and the receiver. Unfortunately, it is extremely difficult to make such a geometry workable, as the receiver picking up the reflection off of the target may be overwhelmed by the far more powerful direct-path signal from the transmitter. In some lucky situations, local geographic features could be exploited to block the direct path interference; for instance, the Manastash Ridge Radar,^{9,10} an FM-radio based passive radar system built by the University of Washington for atmospheric studies, benefits from the presence of Mt. Rainier. However, in general, unless some extremely sophisticated interference estimation and cancellation techniques* are employed, practical imaging systems exploiting tomographic principles may be restricted to the kinds of geometries resulting in the unpleasant PSFs in the top two rows of Fig. 4.

3. EXPERIMENTS WITH CLEAN

In the CLEAN algorithm,⁴ one finds the highest intensity point in the “dirty map” to be CLEANed (or, in the case of complex-valued imagery, the point with the biggest magnitude), shifts the PSF of the system to that point, and normalizes the PSF so that its origin equals the value of the image at the found peak multiplied by a parameter called the *loop gain*. This shifted and normalized PSF is subtracted from the dirty map. A single point, corresponding to where the peak was in the dirty image, is added to a “clean map” which is built up as the algorithm processes. The procedure is iterated until some stopping criteria is met.

3.1. Easy Problems

To help understand the basic operation of the CLEAN approach, in particular the effect of different loops gains, we applied CLEAN to the images shown in Fig. 1. The PSF for this problem is just the inverse Fourier transform of a circular disk of radius 211.25 MHz. The results of CLEAN are shown in the first two rows Fig. 6. The first row corresponds to 2000 iterations with a loop gain of 0.15; the second corresponds to 400 iterations with a loop gain of 0.75. The number of iterations was changed to keep both experiments on a level playing field; note that $2000/400 = 0.75/0.15$.

We ran a similar experiment for the more difficult problem of cleaning the images in the fourth row of Fig. 3. The PSF for this problem is the inverse Fourier transform of a disk of radius 100 MHz. The bottom two rows of Fig. 6 show results of the CLEAN algorithm. Row three shows the result of 1000 iterations with a loop gain of 0.15; row four shows the result of 200 iterations with a loop gain of 0.75.

In both the 211.25 MHz and 100 MHz experiments, we see that the loop gain of 0.75 was overzealous about pulling out peaks, and results in images with a spotty, mottled appearance. Hence, for the remainder of this paper, we employ a loop gain of 0.15. This is consistent with much of the radio astronomy literature, which recommends small loop gains, especially for extended objects.

3.2. Hard Problems

Figure 7 shows the results[†] of 400 iterations of the CLEAN algorithm on the dirty images in Fig. 5. Although CLEAN has excelled in some other high-resolution radar imaging experiments, here, it does not seem to outperform standard direct Fourier reconstruction. In reviewing previous successful applications of CLEAN, it appears that the focus has been on high-frequency imaging. At high-frequencies, the current induced on the target's surface tends to clump at corners, and the resulting images are well-modeled as consisting of distinct separated point scatters, for which the CLEAN algorithm is natural. We see from Figs. 1 and 3 that low-frequency images contain extended structures which bear a striking resemblance to the actual contours of the real aircraft, and are not well-modeled using a small number of scattering centers. However, this explanation cannot be complete, since the radio astronomy literature is full of examples where the CLEAN algorithm produces reasonable results on extended structures such as galaxies. The trouble appears to lie in the complex nature of the underlying radar reflectance and the the PSF which blurs it. Fig. 5 shows that these complex-valued characteristics conspire to obscure true peaks in the underlying reflectance, causing them to be missed by the CLEAN algorithm, and more damagingly creates spurious apparent peaks which mislead the algorithm.

4. FUTURE WORK

The computational experiments in this paper drive home the need for a deconvolution (or equivalently here, a spectral interpolation) technique which does not rely heavily upon the assumption that the target consists of a discrete number of isolated point scatterer. A variety of spectral analysis techniques are reviewed and applied to SAR in Refs. 11 and 12. The GAPES method¹³⁻¹⁹ developed by Larsson, Li, Stoica, Liu and their co-workers seems to be one of the most successful methods to date. We are currently working on applying GAPES to the passive radar imaging problem.

Maximum entropy techniques also invite exploration. Traditional maximum entropy methods enforce a nonnegativity constraint which is appropriate in radio astronomy, but not radar imaging; hence modifications, such as those discussed by Heibreder²⁰ and Borden,^{21,22} are required.

Throughout our simulations, we assumed that the target location, and hence the round-trip distances from the transmitters, to the target, and then to the receivers are known exactly. Of course, this is never precisely known in practice. The uncertainty of path length corresponds to uncertainty in the phase of the measured signal. A small amount of phase error in the Fourier data can corrupt an image beyond all recognition. Autofocus techniques have been the subject of decades of research in SAR, and many thoroughly researched algorithms are regularly applied to real SAR data. However, the passive radar problem presents several difficulties which will require challenging extensions. Autofocus algorithms which rely on finding a bright isolated scatterer and estimating the phase deviations from the pixels surrounding that isolated scatterer may fall prey to the same traps that the CLEAN algorithm did in our experiments above. In traditional active radar systems, range resolution is achieved by transmitted a wideband waveform, so the data may be considered focused in the range dimension; autofocusing is only needed in the cross-range dimension, and hence the problem is one-dimensional. A passive radar system needs to use multiple transmitters and/or receivers to achieve decent resolution, and the associated autofocus problem is inherently two-dimensional. Also, a traditional SAR system, if we may assume perfect focus, has point-spread function which is reasonably well-behaved, unlike the PSFs we see in passive radar systems which can blur objects; having to deal with the sparse sampling effect in conjunction with phase errors can only make both problems harder.

ACKNOWLEDGMENTS

This work was supported by a grant from DARPA under Contract F49620-98-1-0498, administered by AFOSR. We would like to thank Dick Ludwig, Bert Bradford, and Bob Taylor of Lockheed Martin Mission Systems for many helpful discussions.

*The specific applications of such techniques to passive radar seems to be largely unexplored territory, and is ripe for future research.

[†]The raw CLEAN images are sparse and may be difficult to reproduce in print in their original state. Hence, the magnitudes of the radar images have been blurred by a Gaussian kernel, and the images are displayed on a square-root scale to make sure that faint features appear after copying.

REFERENCES

1. D. Munson and J. Sanz, "Image reconstruction from frequency-offset fourier data," *Proceedings of the IEEE* **72**, pp. 661–669, June 1984.
2. O. Arikan and D. Munson, "A tomographic formulation of bistatic synthetic aperture radar," in *Proceedings of ComCon 88: Advances in Communications and Control Systems*, October 19–21 1998.
3. D. Mensa and G. Heidbreder, "Bistatic synthetic-aperture radar imaging of rotating objects," *IEEE Trans. on Aerospace and Electronic Systems* **18**, pp. 423–431, July 1992.
4. J. Högbom, "Aperture synthesis with a non-regular distribution of interferometer baselines," *Astronomy and Astrophysics Supplement Series* **15**, pp. 417–426, 1974.
5. U. Schwarz, "Mathematical-statistical description of the iterative beam removing technique (method CLEAN)," *Astronomy and Astrophysics* **65**, pp. 345–356, 1978.
6. J. Ables, "Maximum entropy spectral analysis," *Astronomy and Astrophysics Supplement Series* **15**, pp. 383–393, 1974.
7. J. Ponsonby, "An entropy measure for partially polarized radiation and its application to estimating radio sky polarization distributions from incomplete "aperture synthesis" data by the maximum entropy method," *Monthly Notices of the Royal Astronomical Society* **163**, p. 1973, 369–380.
8. Y. Wu and D. Munson, "Multistatic synthetic aperture imaging of aircraft using reflected television signals," in *Algorithms for Synthetic Aperture Radar Imagery VIII*, E. Zelnio, ed., vol. SPIE Proc. 4382, (Orlando, FL), April 2001.
9. J. Sahr and F. Lind, "The Manastash ridge radar: A passive bistatic radar for upper atmospheric radio science," *Radio Science*, pp. 2345–2358, Nov.–Dec. 1997.
10. J. Sahr and F. Lind, "Passive radio remote sensing of the atmosphere using transmitters of opportunity," *Radio Science*, pp. 4–7, March 1998.
11. D. Pastina, A. Farina, J. Gunning, and P. Lombardo, "Two-dimensional super-resolution spectral analysis applied to SAR images," *IEE Proc. F: Radar Sonar, and Navigation* **145**, pp. 281–290, Oct. 1998.
12. S. DeGraaf, "SAR imaging via modern 2-D spectral estimation methods," *IEEE Trans. on Signal Processing* **7**, pp. 729–761, May 1998.
13. J. Li and P. Stoica, "An adaptive filtering approach to spectral estimation and SAR imaging," *IEEE Trans. on Signal Processing* **44**, pp. 1469–1484, June 1996.
14. H. Li, J. Li, and P. Stoica, "Performance analysis of forward-backward matched-filterbank spectral estimators," *IEEE Trans. on Signal Processing* **46**, pp. 1956–1966, July 1998.
15. P. Stoica, H. Li, and J. Li, "A new derivation of the APES filter," *IEEE Signal Processing Letters* **6**, pp. 205–206, Aug. 1999.
16. P. Stoica, E. Larsson, and J. Li, "Adaptive filterbank approach to restoration and spectral analysis of gapped data," *The Astronomical Journal* **120**, pp. 2163–2173, Oct. 2000.
17. E. Larsson, G. Liu, P. Stoica, and J. Li, "High-resolution SAR imaging with angular diversity," *IEEE Trans. on Aerospace and Electronic Systems* **37**, pp. 1359–1372, Oct. 2001.
18. E. Larsson and P. Stoica, "Fast implementation of two-dimensional apes and capon spectral estimators," *Multidimensional Systems and Signal Processing* **13**(1), pp. 35–54, 2002.
19. E. Larsson, P. Stoica, and J. Li, "Amplitude spectrum estimation for two-dimensional gapped data," *IEEE Trans. on Signal Processing*. to appear.
20. G. Heidbreder, "Maximum entropy methods in coherent radar imaging," *International Journal of Imaging Systems and Technology* **2**, pp. 239–247, 1990.
21. B. Borden, "Maximum entropy regularization in inverse synthetic aperture radar imagery," *IEEE Trans. on Signal Processing* **40**, pp. 969–973, April 1992.
22. B. Borden, "Regularization of noisy ISAR images containing extended features," *IEEE Trans. on Image Processing* **8**, pp. 124–127, Jan. 1999.

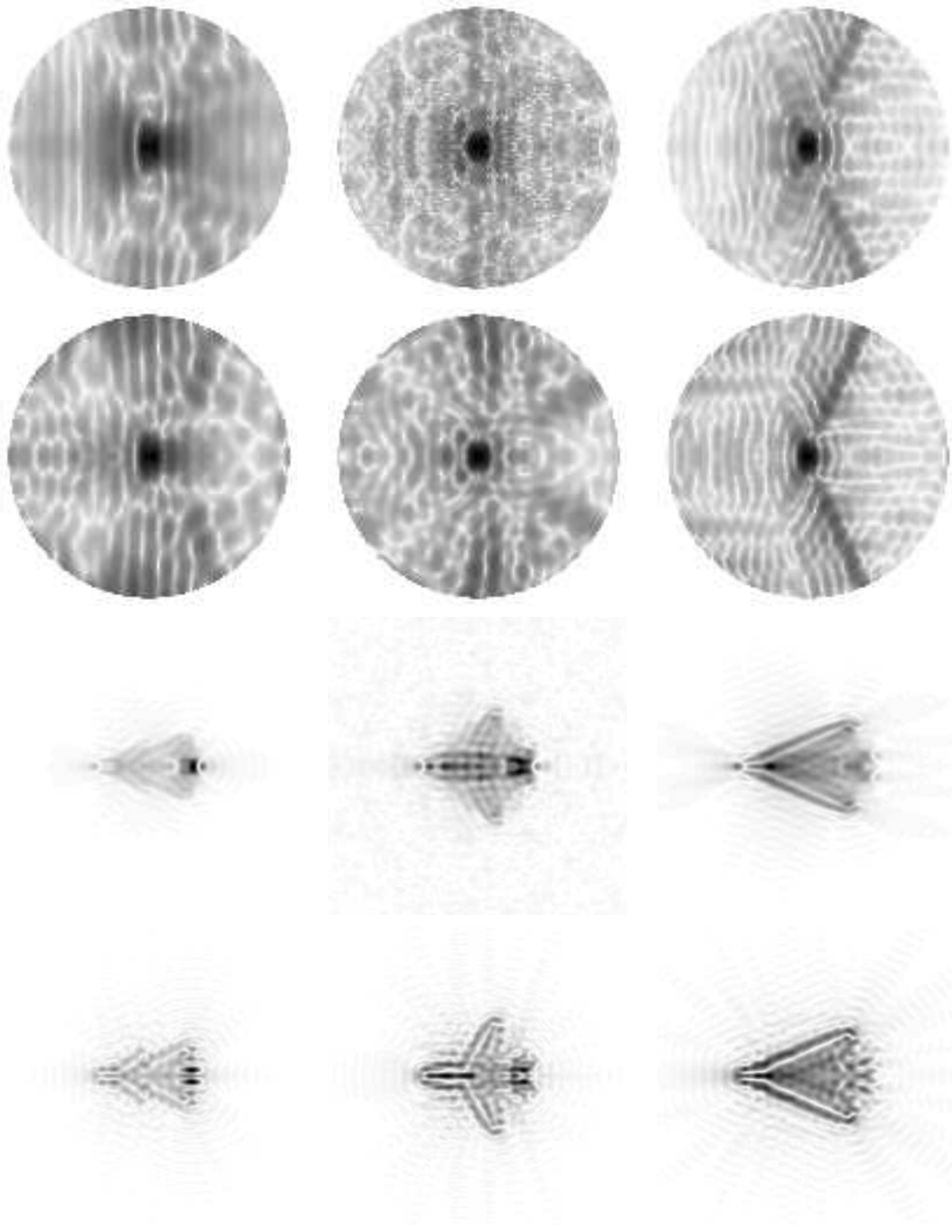


Figure 3. First row shows approximate Fourier data for a 100 MHz signal, synthesized by windowing a Fourier dataset generated with a 211.25 MHz signals. Second row shows Fourier data for an actual 100 MHz signal. Bottom two rows show corresponding radar images (third row for approximate 100 MHz dataset, fourth row for true 100 MHz data set) created using direct Fourier reconstruction. Left to right: VFY-218, Falcon 20, Flying Bat. The actual images are 512×512 ; here only the middle 256×256 pixels are shown.

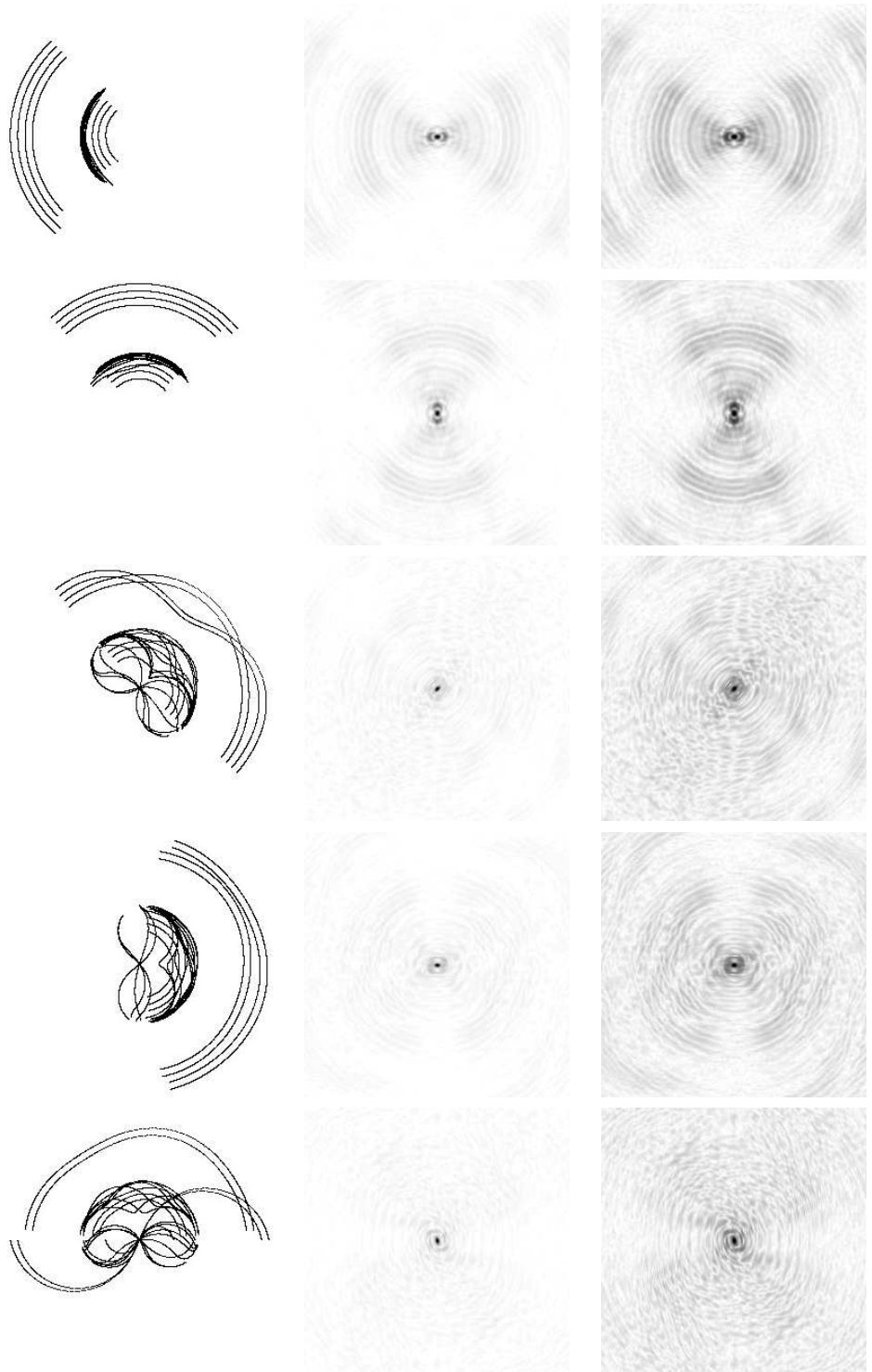


Figure 4. Left column shows Fourier sampling patterns associated with five different flight paths. Remaining columns show the magnitude of the PSFs associated with the sampling patterns. The middle column uses a linear scale, while the right column uses a logarithmic scale to show fine detail. The actual PSFs are 512×512 ; here only the middle 256×256 pixels are shown.

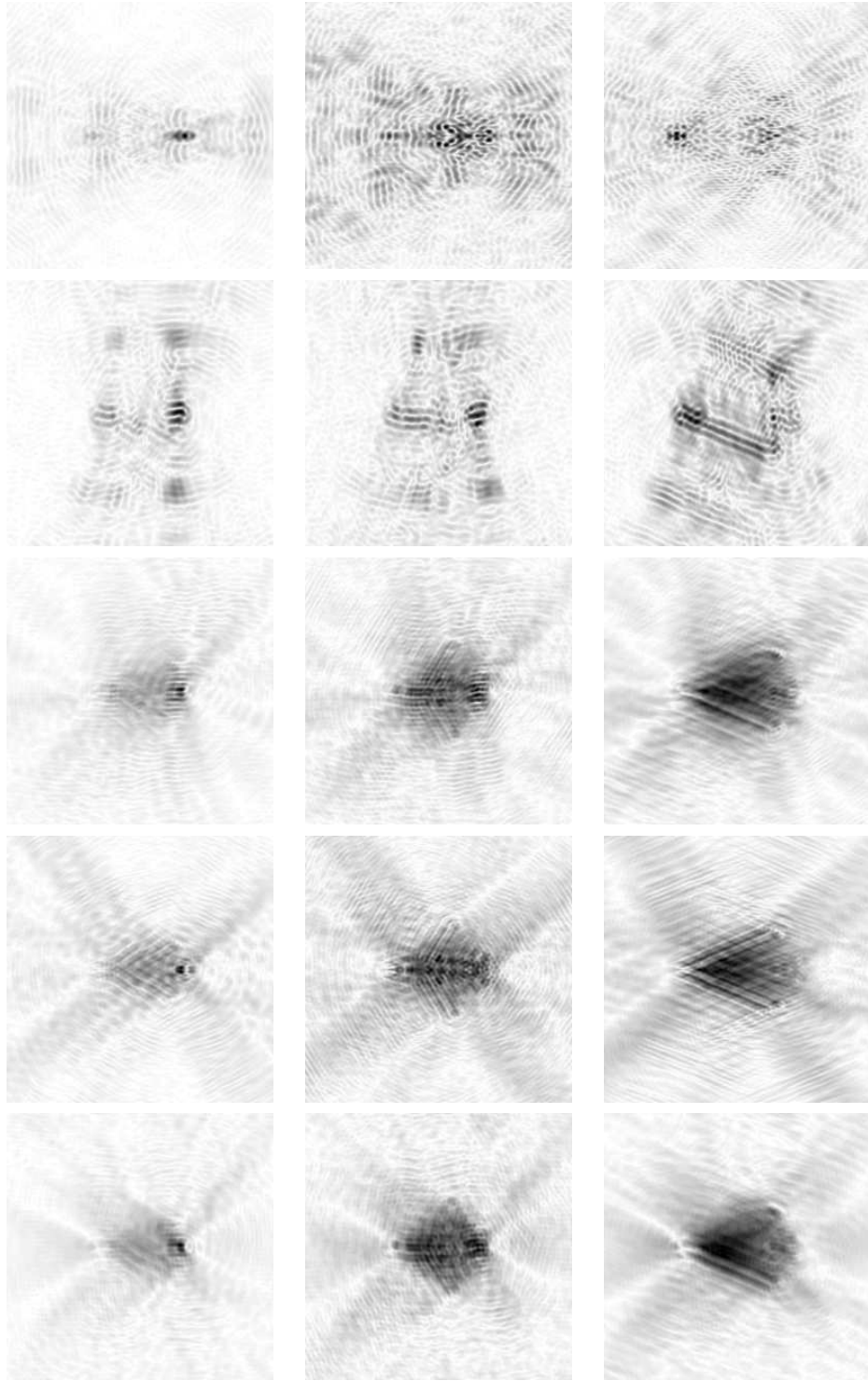


Figure 5. Direct Fourier reconstruction using data restricted to the Fourier sampling patterns shown in Fig. 4. Left to right: VFY-218, Falcon 20, Flying Bat.

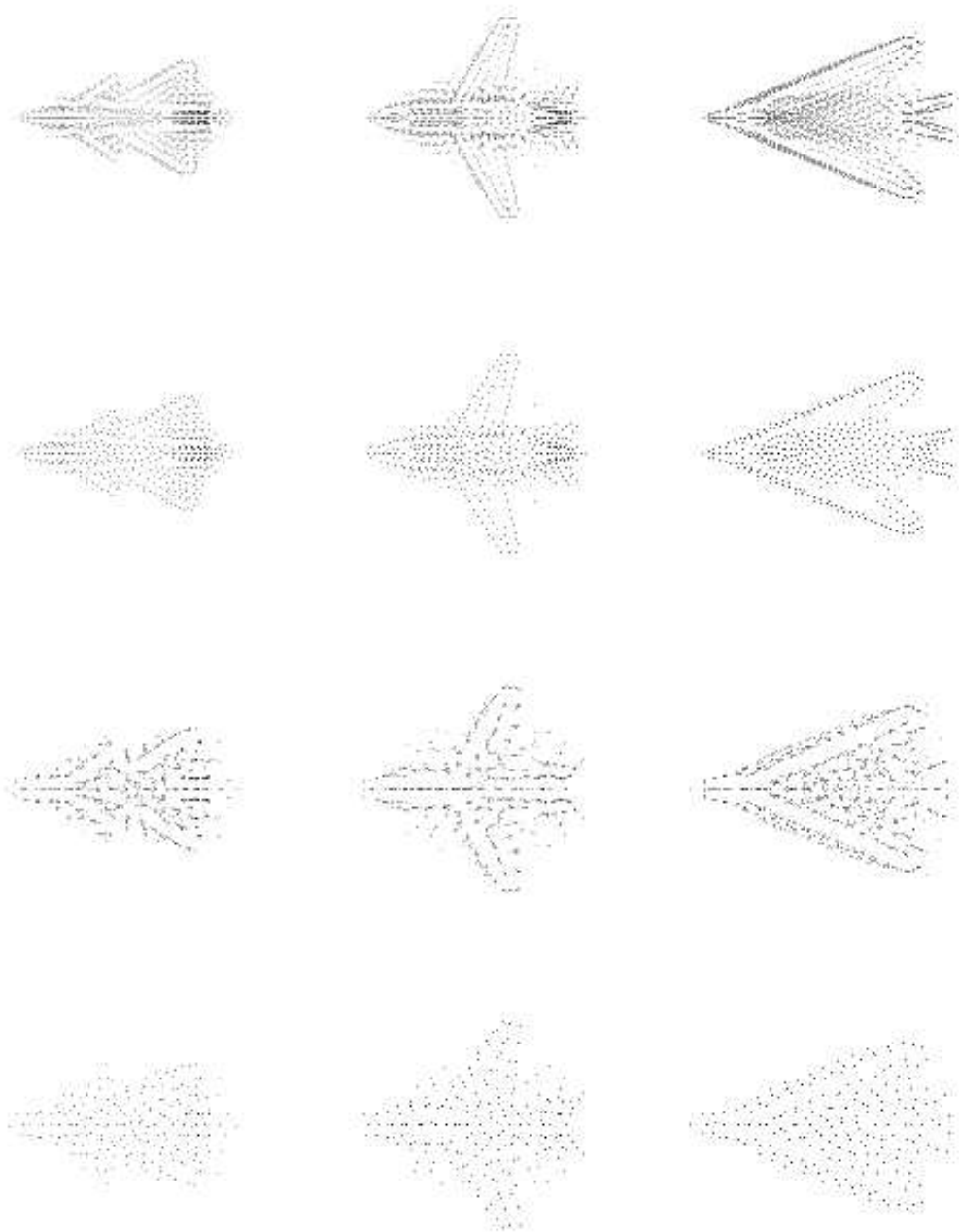


Figure 6. Results of applying the CLEAN algorithm to ideal full-disk Fourier datasets, for FISC runs at 211.25 MHz (top two rows) and 100 MHz (bottom two rows). First row: 2000 iterations, loop gain 0.15. Second row: 400 iterations, loop gain 0.75. Third row: 1000 iterations, loop gain 0.15. Fourth row: 200 iterations, loop gain 0.75.

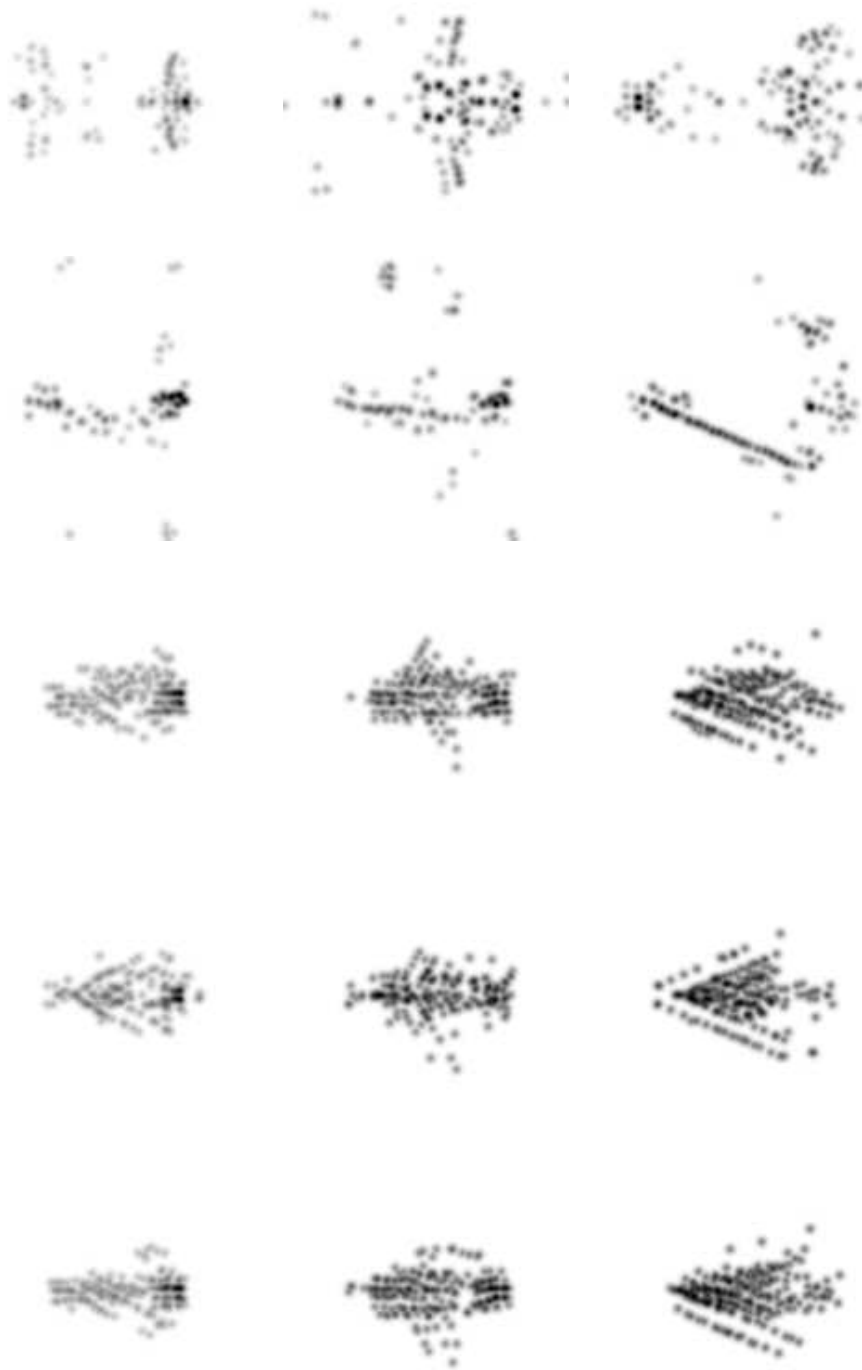


Figure 7. Results of applying 400 iterations of the CLEAN algorithm with a loop gain of 0.15 to the images of Fig. 5.